Probabilistic assessment of potential fault slip related to injection-induced earthquakes: Application to north central Oklahoma, USA

Walsh and Zoback

SUPPLEMENTARY MATERIAL

Mohr-Coulomb Slip Calculation

A recent summary of Mohr-Coulomb slip Criteria as it applies to injection induced seismicity, is available in (NRC 2012). For a given fault in a given stress field, we resolve the stress tensor on the fault, to calculate shear stress and normal stress. The Mohr-Coulomb slip failure criteria is our limit state function, which states that slip occurs if:

$$\tau \geq \mu (S_n - P_p)$$

where τ is the resolved shear stress on the fault, μ is the coefficient of friction, S_n is the normal (compressive) stress on the fault, and P_p is the pore pressure (Twiss and Moores, 1992). Thus in a deterministic way, we can straightforwardly calculate the pore pressure calculation that would be required to make an otherwise stable fault slip. In the QRA, we iterate the Mohr-Coulomb calculation with random samples from a distribution of each relevant parameter, reflecting its uncertainty. The distribution of outputs allows us to calculate the probability that a specific increase in pore pressure would cause fault slip. It should be noted that mechanisms of injection induced seismicity remain a field of ongoing research, and while we believe that this calculation is the simplest and most applicable, there are also other physical processes that could be relevant to triggering that we do not assess. These include poroelastic and thermoelastic stressing, rate and state-dependent frictional thresholds and stress-driven creep. It is also possible that faults have some cohesion, however it is unclear if it is significant when compared to uncertainty in friction coefficient and don't model it in this study, but it could be explicitly modeled in future work.

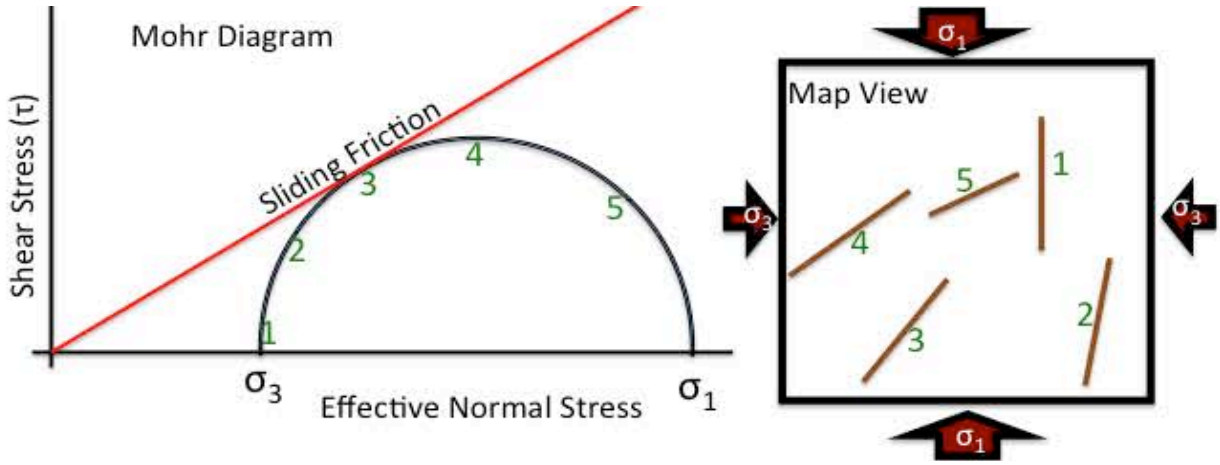

Figure DR1: 2D Mohr diagram showing 5 hypothetical faults in a 2D Mohr circle numbered to correspond to their orientations on the map. Fault number 3 is closest to slip in this stress field because the ratio of shear to effective normal stress is highest. Faults 2 and 4 could be triggered by modest changes in pore pressure, and faults 1 and 5 would require the most pore pressure to slip.

Application to Hydraulic Fracturing Seismicity

Although earthquakes of magnitude 2 and larger rarely occur during hydraulic fracturing, the methodology discussed here could also be used to assess the potential for fault slip during hydraulic fracturing (e.g. Friberg et al. 2015; Holland, 2013). Larger pore pressure perturbations would be expected during hydraulic fracturing operations than the < 2 MPa pore pressure change considered here for water disposal. To consider the probability that hydraulic fracturing might trigger slip, Fig. 3C considers the potential for slip on faults that might experience pressure changes as high as the magnitude of the least principal stress (sometimes referred to as the fracture gradient). Unlike saltwater disposal, hydraulic fracturing operations affect a small volume of rock for a short period of time. For example, during multi-stage hydraulic fracturing

in a horizontal well, it is typical to pressurize a ~100m long section of a well for about two hours.

Inversion of Moment Tensors for Stress

Study Area	S_{Hmax} Azimuth and Standard Deviation	ϕ	Number of Focal Mechanisms	Stress State
1	83 ±2°	0.93 ± 0.04	65	Strike Slip and Normal Faulting
2N	73±6°	0.65 ± 0.1	33	Normal Faulting
2S	NA	NA	33	Strike Slip and Normal Faulting
3	82 ±1°	0.82 ± 0.04	132	Strike Slip Faulting
4	82 ±4°	0.74 ± 0.12	28	Strike Slip Faulting
5	83 ± 2°	0.72 ± 0.06	51	Strike Slip Faulting
6	84 ±2°	0.62 ± 0.09	26	Strike Slip Faulting

Table DR1: Moment Tensor inversion Results for each area.

Figures DR2-DR8 below show the evolution of S_{Hmax} azimuth (A) and ϕ (B) through time in each study area as more earthquakes occur. For a group of earthquake focal plane mechanisms, the inversion finds the best-fitting uniform stress orientation and relative magnitude by minimizing the misfit between the predicted and observed slip vectors on each of the nodal planes of the focal mechanism. The black line shows the deterministic result of 1 inversion of all moment tensors in the area up to that point in time, and the yellow to blue shows the density distribution of 1000 bootstrapped inversions of moment tensors up to that time. As more earthquakes occur with time, the inversion stabilizes (generally by 25-30 events), and the distribution and range of bootstrapped uncertainties tightens around the deterministic result. Also shown as magenta dashed lines (panel A) are the azimuths of S_{Hmax} from independent wellbore measurements (Alt and Zoback 2014, Heidbach et al. 2010) and the count of moment tensors through time in orange (right axis).

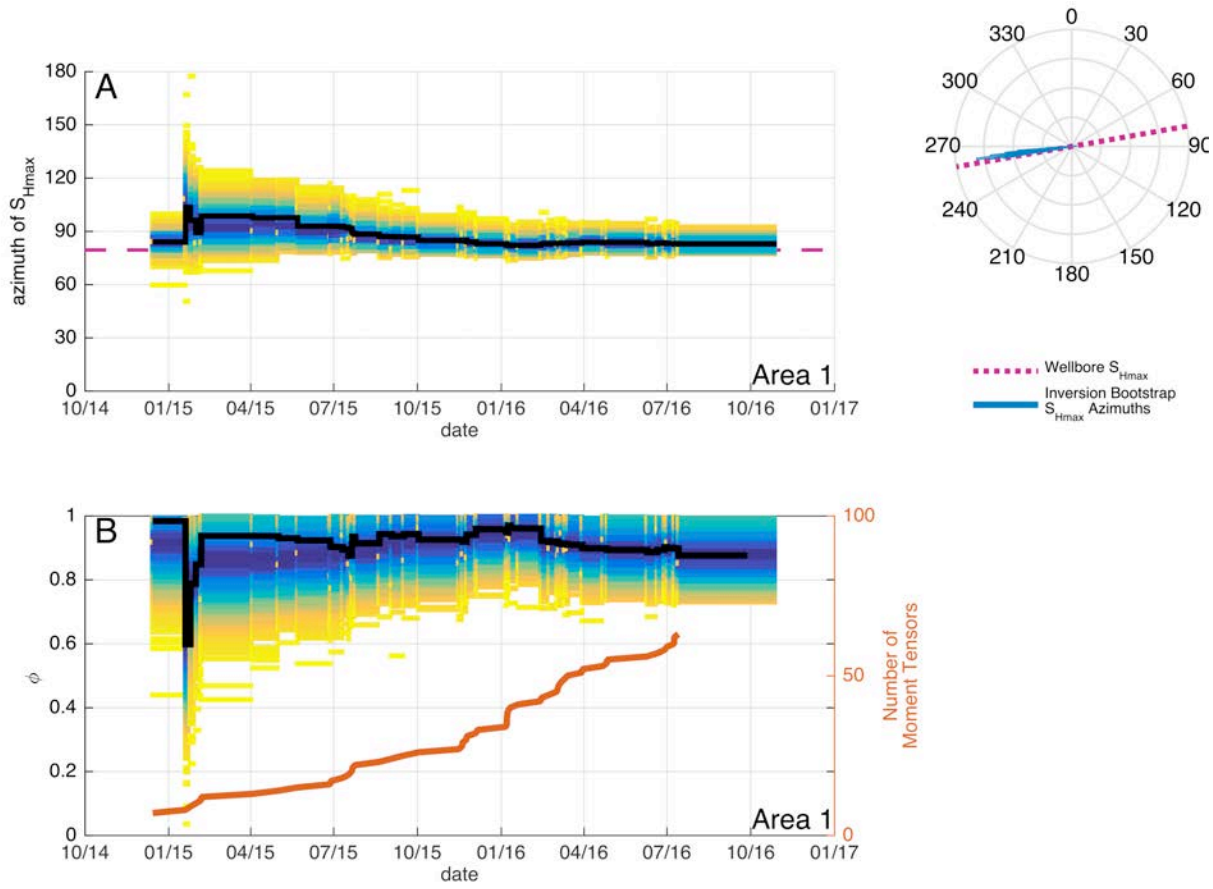

Figure DR2. Bootstrapped Inversion results through time as more earthquakes occur in area 1. Black is the deterministic inversion result, and blue-yellow shows the density of bootstrapped results through time. The magenta dashed line shows the S_{Hmax} azimuth from a wellbore measurement in area 1. The inversion converges to match the wellbore measurement. In DR2B, the orange line indicates the number of earthquakes with moment tensors used in the inversion as a function of time. A rose diagram is also shown with the final S_{Hmax} azimuths from the final bootstrapped results in blue, and the wellbore measurement as a magenta dashed line.

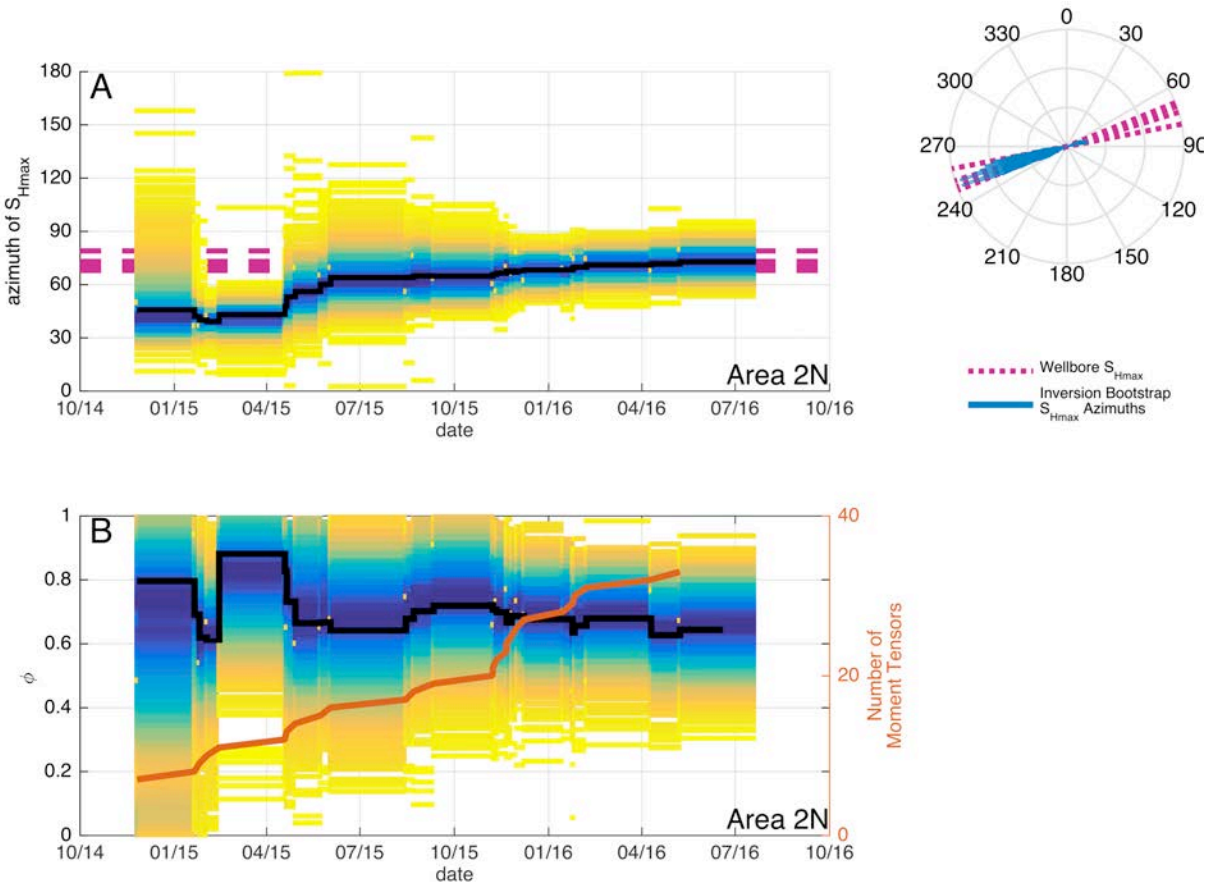

Figure DR3. Bootstrapped Inversion results through time as more earthquakes occur in area 2N. Black is the deterministic inversion result, and blue-yellow shows the distribution of bootstrapped results through time. The orange line indicates the number of earthquakes with moment tensors used in the inversion as a function of time. The horizontal magenta dashed lines show the S_{Hmax} azimuths from wellbore measurements. The inversion converges to match the wellbore measurements. A rose diagram is shown with the final S_{Hmax} azimuths from the final bootstrapped results in blue, and the wellbore measurements as magenta dashed lines.

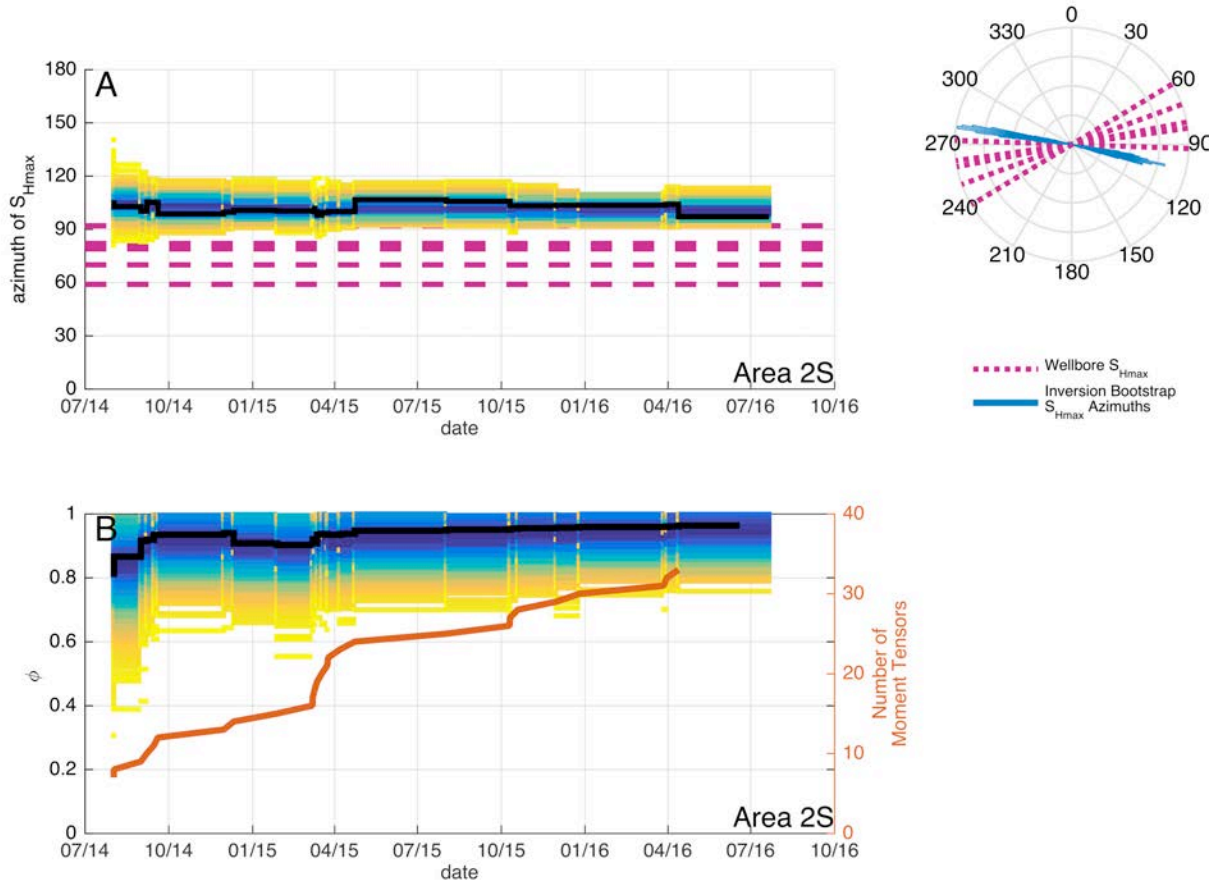

Figure DR4. Bootstrapped Inversion results through time as more earthquakes occur in area 2S. Black is the deterministic inversion result, and blue-yellow shows the distribution of bootstrapped results through time. The orange line indicates the number of earthquakes with moment tensors used in the inversion as a function of time. The horizontal magenta dashed lines show the S_{Hmax} azimuths from wellbore measurements (Alt and Zoback 2014, Heidbach et al. 2010). Here, the earthquake inversion does not converge to the wellbore measurements. A rose diagram is shown with the final S_{Hmax} azimuths from the final bootstrapped results in blue, and the wellbore measurements as magenta dashed lines, which clearly don't agree. This may because the stress orientation changes with depth, as the earthquakes are considerably deeper than the wells, or because there are insufficient earthquakes in the inversion. Whatever the

reason, because the geomechanical uncertainties are large and the inversion can't be verified, we do not present fault results for this area in figure 4.

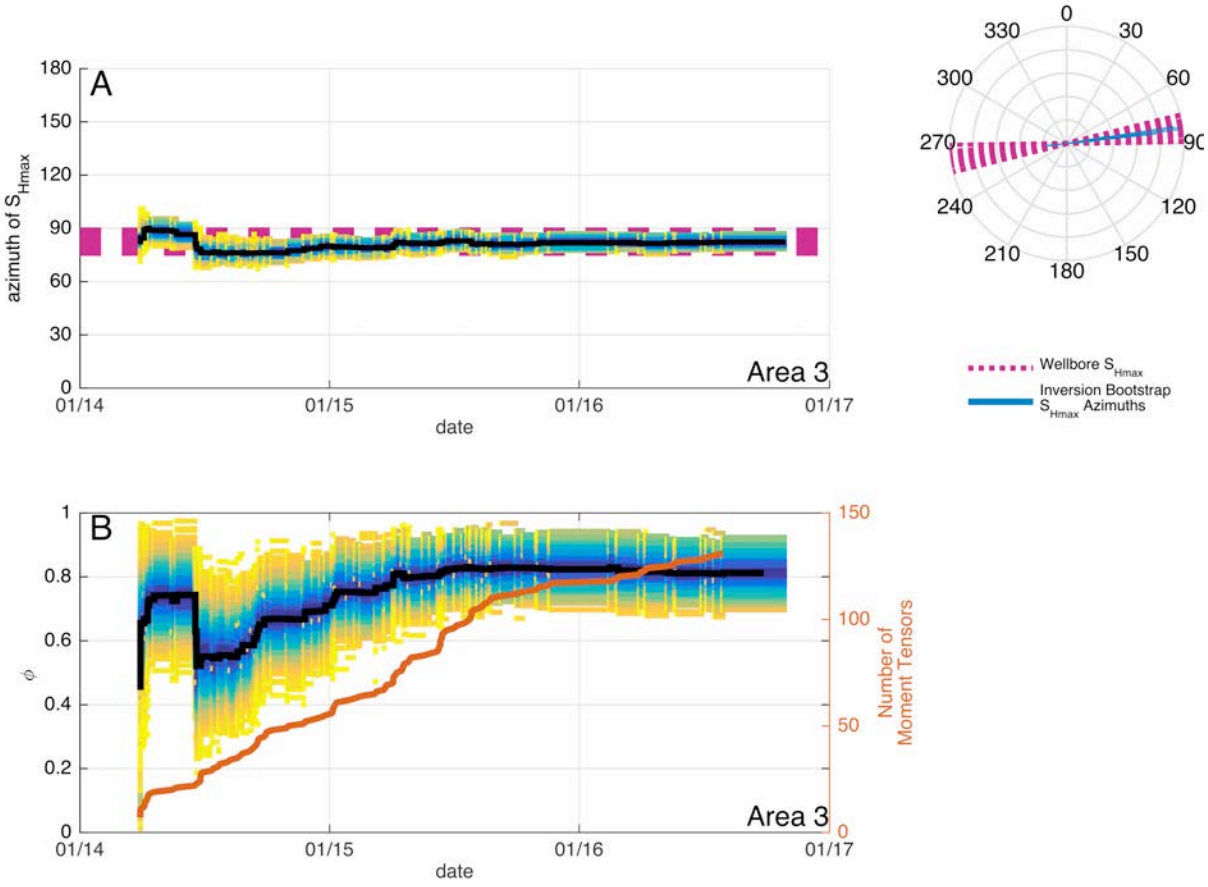

Figure DR5. Bootstrapped inversion results through time as more earthquakes occur in area 3. Black is the deterministic inversion result, and blue-yellow shows the distribution of bootstrapped results through time. The orange line indicates the number of earthquakes with moment tensors used in the inversion as a function of time. The horizontal magenta dashed line shows the S_{Hmax} azimuths from wellbore measurements. The inversion converges to match the wellbore measurements, and here the wellbore measurements have a greater variation than the inversions.

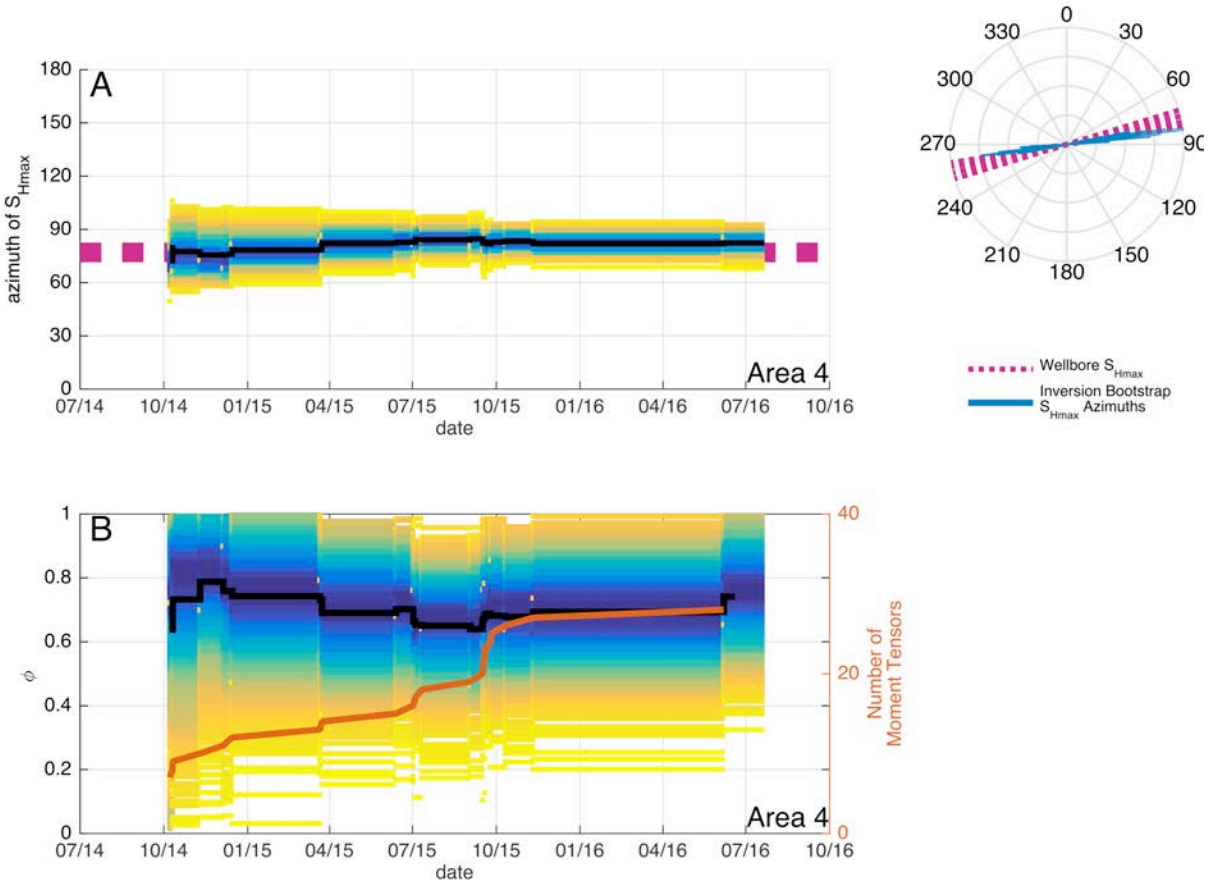

Figure DR6. Bootstrapped Inversion results through time as more earthquakes occur in area 4. Black is the deterministic inversion result, and blue-yellow shows the distribution of bootstrapped results through time. The orange line indicates the number of earthquakes with moment tensors used in the inversion as a function of time. The horizontal magenta dashed line shows the S_{Hmax} azimuths from wellbore measurements. The inversion converges to match the wellbore measurements.

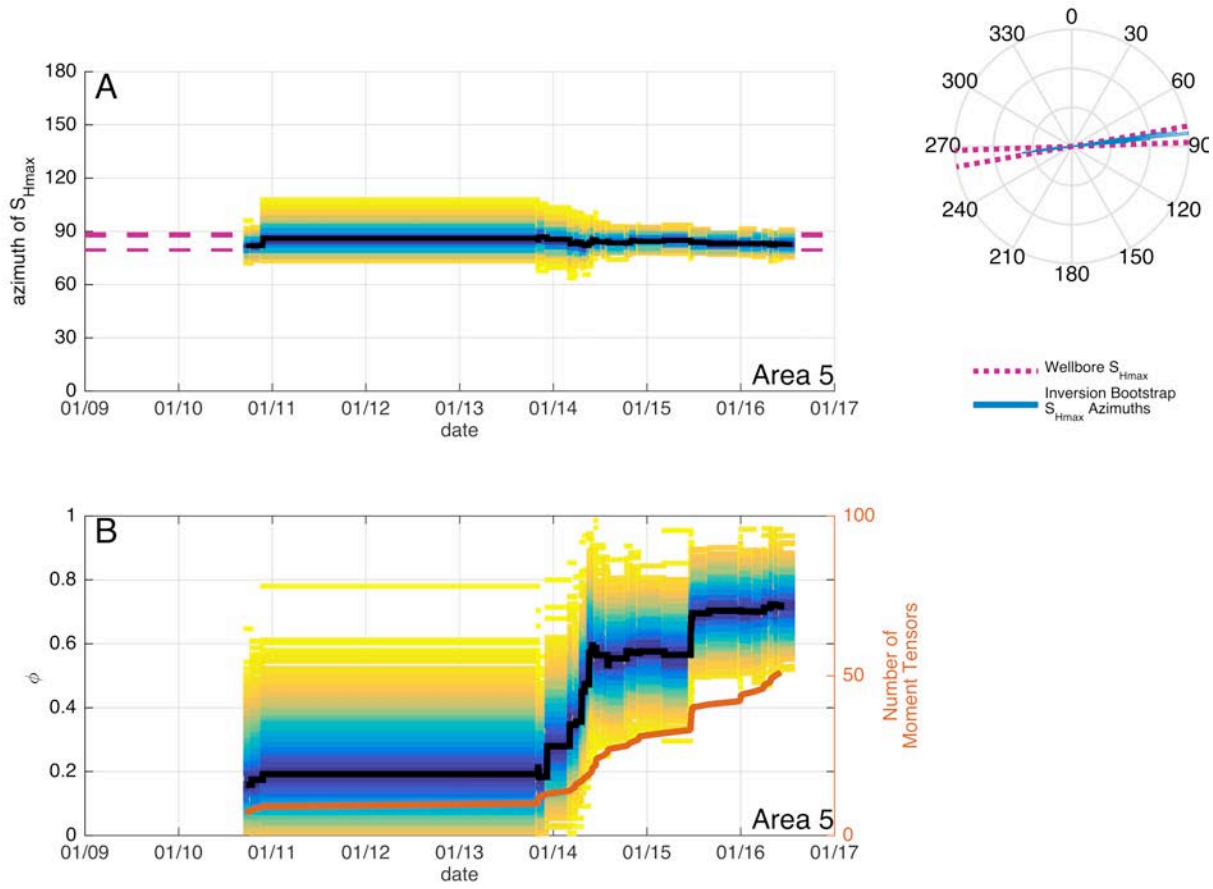

Figure DR7. Bootstrapped Inversion results through time as more earthquakes occur in area 5. Black is the deterministic inversion result, and blue-yellow shows the distribution of bootstrapped results through time. The orange line indicates the number of earthquakes with moment tensors used in the inversion as a function of time. The horizontal magenta dashed line shows the S_{Hmax} azimuths from wellbore measurements. The inversion converges to right between the two wellbore measurements.

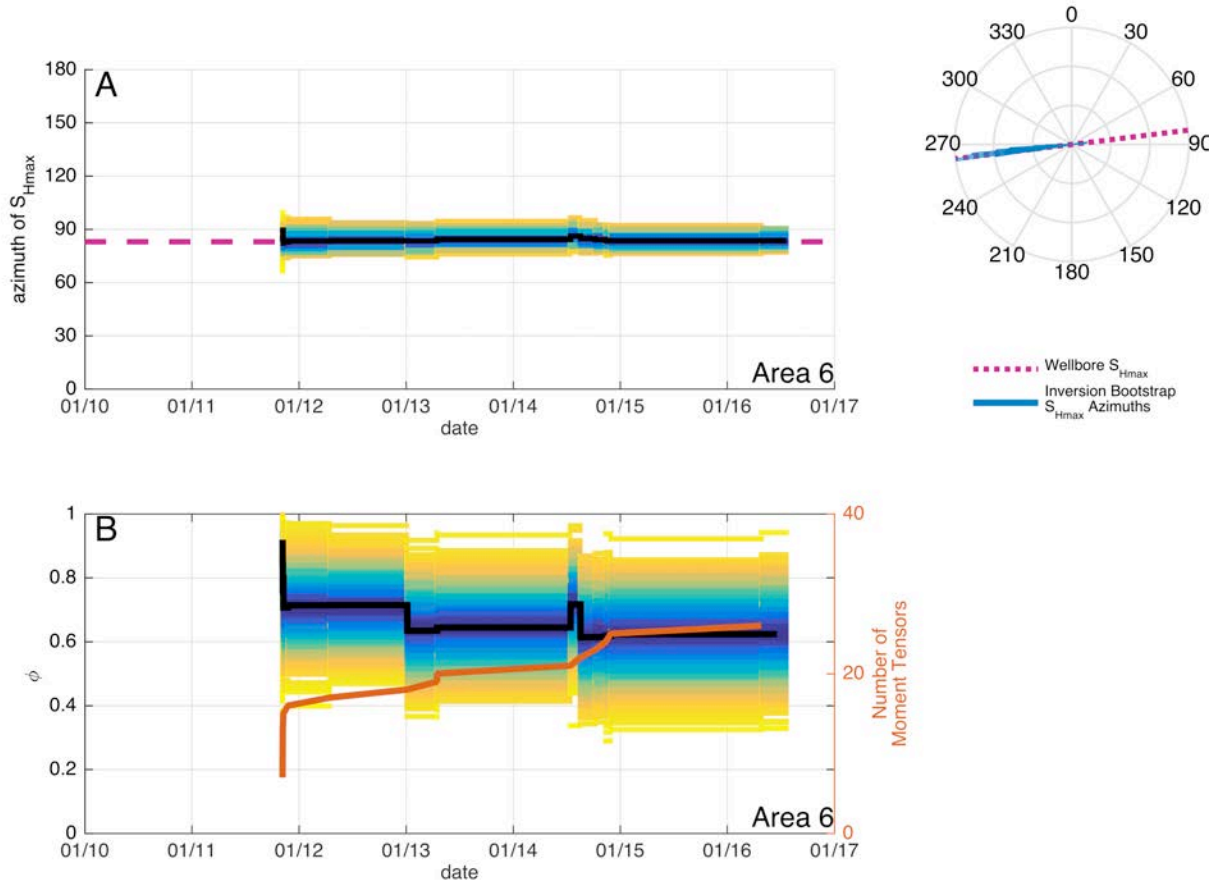

Figure DR8. Bootstrapped Inversion results through time as more earthquakes occur in area 6. Black is the deterministic inversion result, and blue-yellow shows the distribution of bootstrapped results through time. The orange line indicates the number of earthquakes with moment tensors used in the inversion as a function of time. The horizontal magenta dashed line shows the S_{Hmax} azimuths from wellbore measurements. The inversion converges to match the wellbore measurement.

Constraining Geomechanical Parameters and Their Uncertainties

The QRA propagates uncertainties in the geomechanical parameters, and it is thus only as good as the constraints in those parameters are. Here we describe how we constrain each distribution, as shown in Figure 2 for area 6, and Figures DR 9-DR13 for the other areas. The

friction distribution (Plot A) is taken from laboratory friction measurements on wet Westerly granite (Blanpied et al. 1995) at pressure and temperature. It would be ideal to have laboratory testing of the actual rock in question, but this is not available. The overburden gradient distribution (Plot G) is estimated from typical densities of sediments. The S_{Hmax} and S_{hmin} magnitude distributions (Plots F and H) are calculated from the overburden gradient, pore pressure, ϕ, and coefficient of friction, assuming that pore pressure perturbations of less than 2 MPa are inducing slip on the faults that are most favorably oriented for failure in the current stress field. 2 MPa is a likely upper bound for pressure changes in the Arbuckle formation from wastewater injection because wellhead pressures rapidly return to subhydrostatic values after pumping stops (Nelson et al. 2015). The natural pore pressure distribution (Plot E) is uniform based on bounds from Nelson et al. (2015). Calculations are done for a depth of 5 km, the depth of most of the earthquakes in the area (McNamara et al., 2015). The distribution of fault strike (Plot D) represents the fault segments mapped within the study area with Gaussian noise of standard deviation of 2 degrees (and truncated at 5 degrees) added to each mapped strike. This can simulate non-planarity of the fault or uncertainty in mapping. Fault strikes also randomly flip 180 degrees to maintain a right hand rule between strike and dip direction, as absent constraining information, the fault can dip either direction relative to the mapped fault segment. The fault dip distribution (Plot C) is designed to sample reasonable dips of possibly active faults in a given stress state. Table DR2 shows uncertainties associated with each parameter for area 6. The main difference between these distributions in the other areas is that the unconstrained dip distribution was designed to sample the dips of active faults in in the stress state of each area.

Table DR2. Data distributions for Area 6.

Parameter	Distribution	Mean Value	Standard Deviation	Bounds	Notes
Coefficient of friction	Truncated Gaussian	0.71	0.026	0.62 to 0.82	Distribution of 23 Measurements from Blanpied et al. (1995)
Phi	Inversion bootstrap result	0.622	0.089	0.26 to 0.96	From Moment Tensor Inversion
Fault dip	Truncated Gaussian	89	10	0 to 90 degrees	Designed to sample strike-slip fault dips
Fault strike	From Map	Mapped Value	2 degrees	+/- 5 degrees	Noise added to simulate non-planarity or map uncertainty
Pore pressure	Uniform	N/A	N/A	45.2 to 50.9 MPa	Bounds from Nelson et al. (2015)
S_{hmin}	Calculated	76.6	3.18	67.0 to 91.7 MPa	Calculated from other parameters assuming frictional equilibrium
Overburden Gradient	Calculated	125	2.78	114.4 to 135.8 MPa	Based on assumed rock density
S_{Hmax}	Calculated	155.42	10.76	125.3 to 217.7 MPa	Calculated from other parameters assuming frictional equilibrium
Stress orientation	Inversion bootstrap result	N/A	N/A	N/A	From Moment Tensor Inversion

The following figures show Monte Carlo input distributions (as in Figure 3), for study areas other than Area 6.

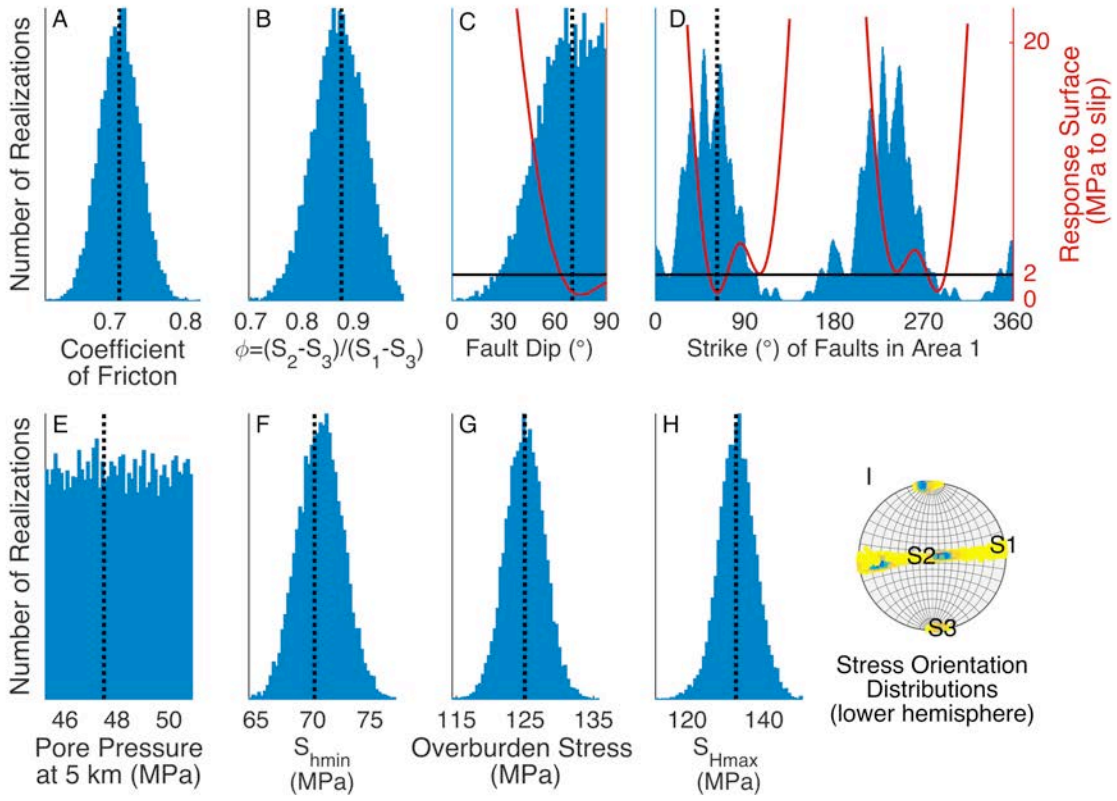

Figure DR9. Data distributions and strike and dip response surfaces for area 1. Because this is a strike slip/normal faulting transitional stress state, S1 and S2 can each be the steeper dipping principal stress, as evidenced by the girdle on the stereonet (I).

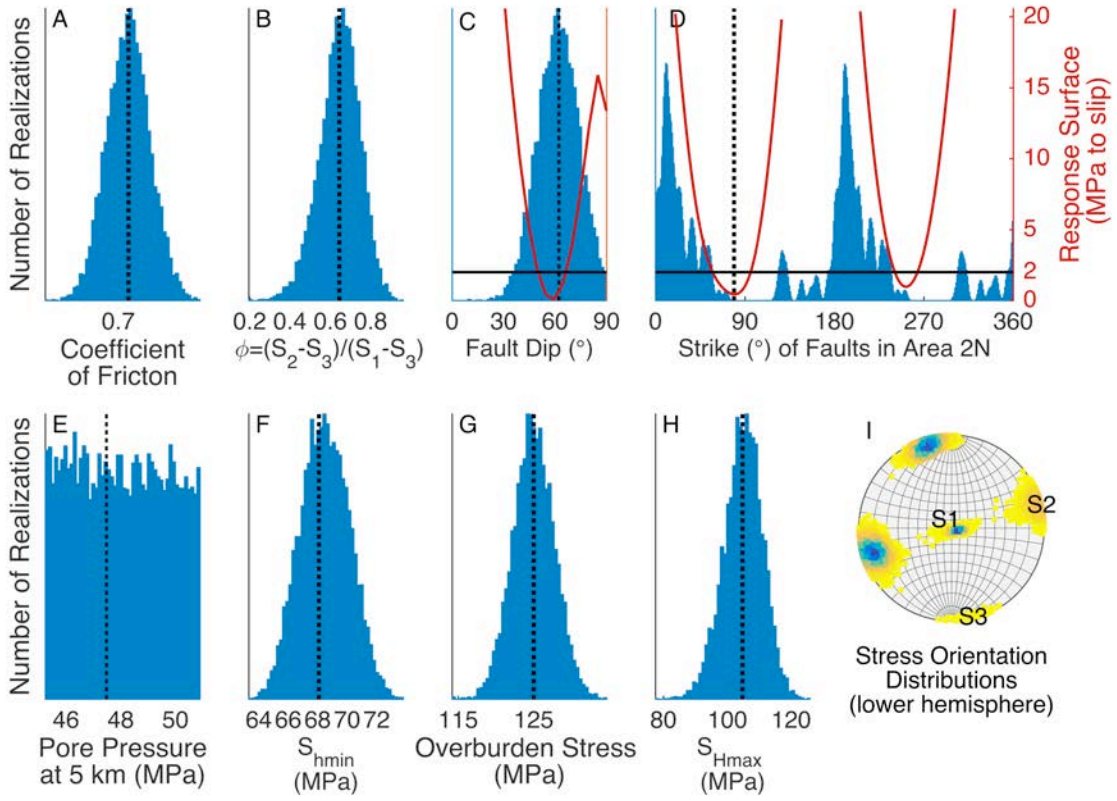

Figure DR10. Data distributions and strike and dip response surfaces for area 2N.

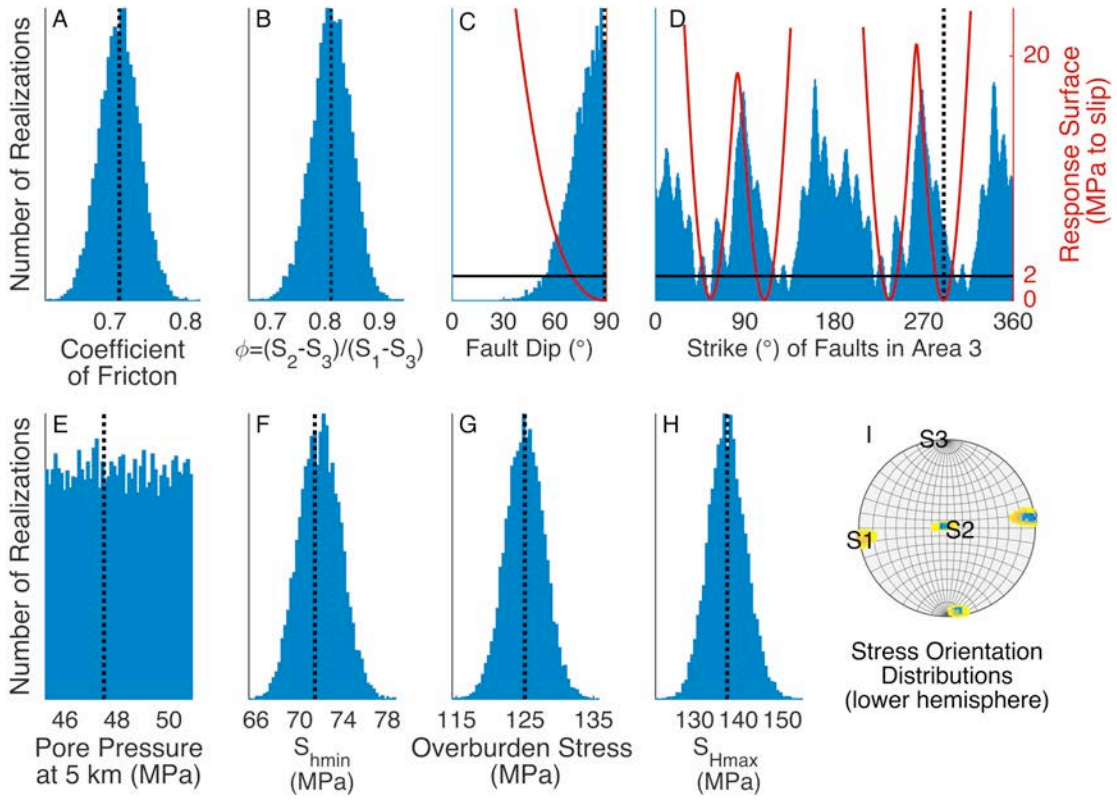

Figure DR11. Data distributions and strike and dip response surfaces (red) for area 3.

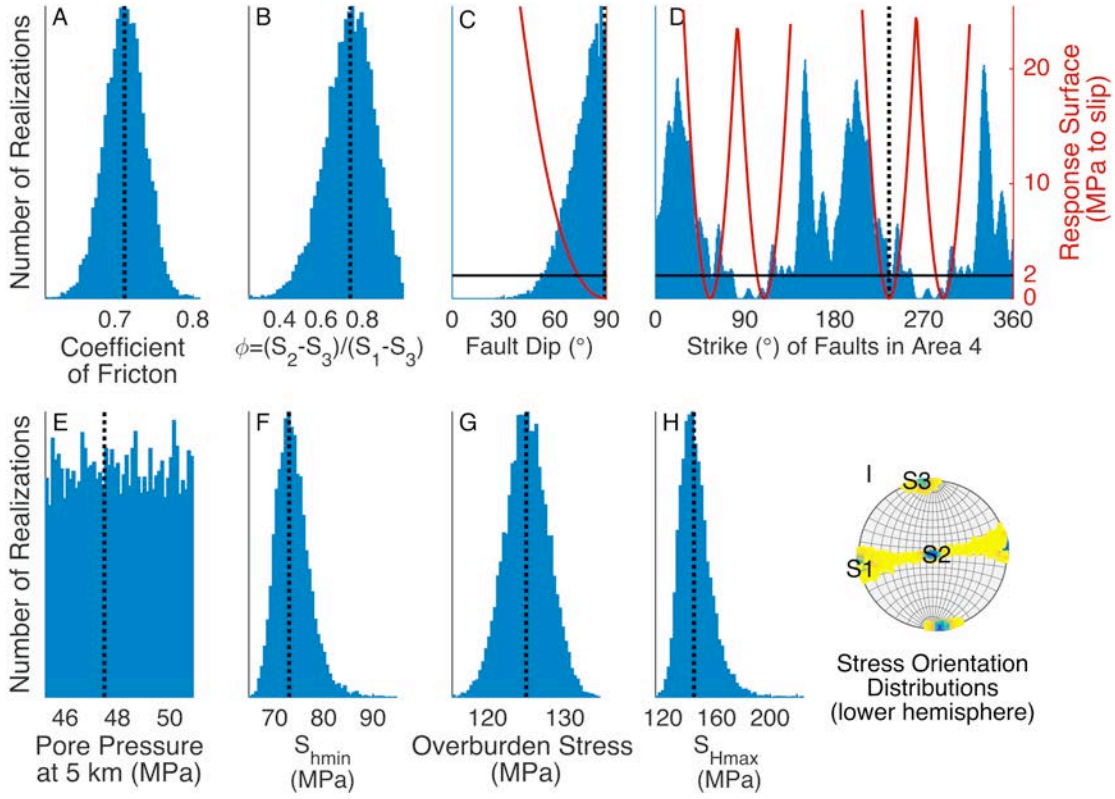

Figure DR12. Data distributions and strike and dip response surfaces (red) for area 4.

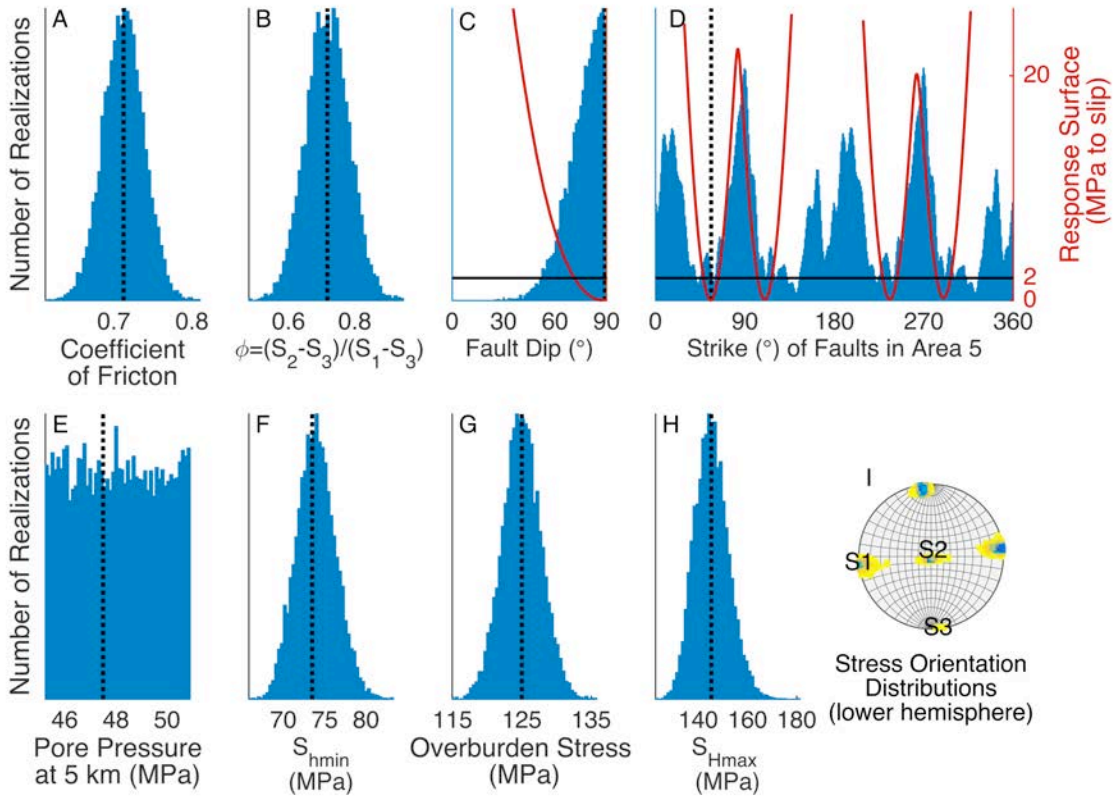

Figure DR13. Data distributions and strike and dip response surfaces for area 5.

Below are traffic light colored mapped faults in each study area (A), and their corresponding CDF curves in B. Panel C extends the pressure axis to pressure ranges that would be more applicable to hydraulic fracturing induced seismicity and shows the fracture gradient.

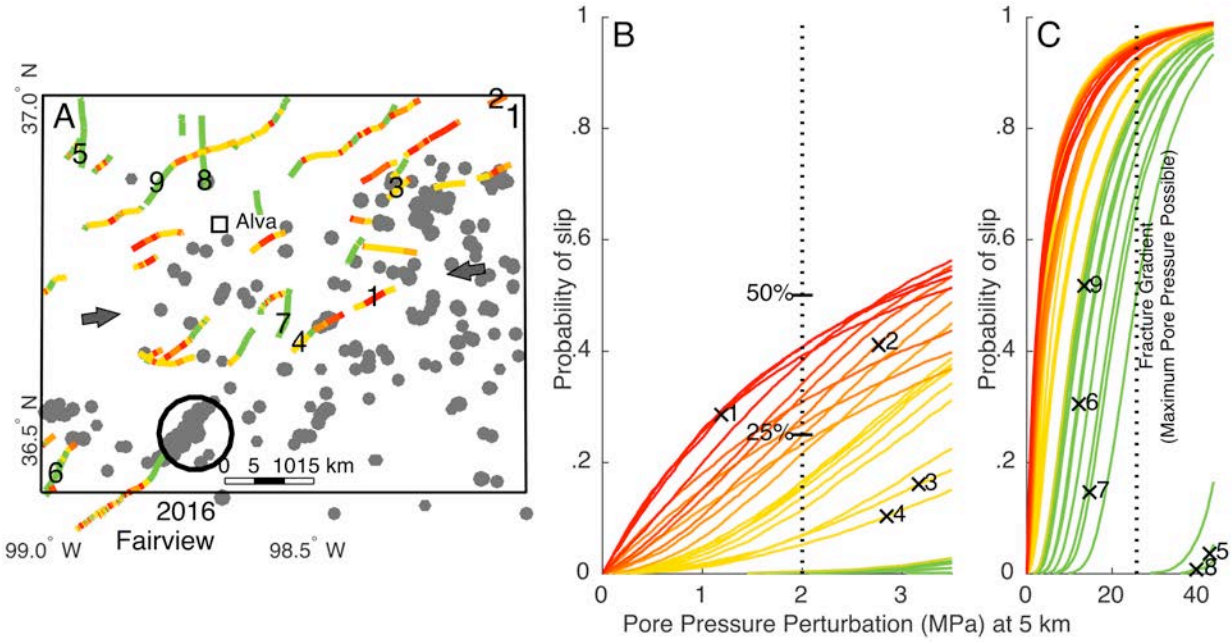

Figure DR14. Faults, NEIC earthquakes (A), and CDF curves (B, C) for area 1.

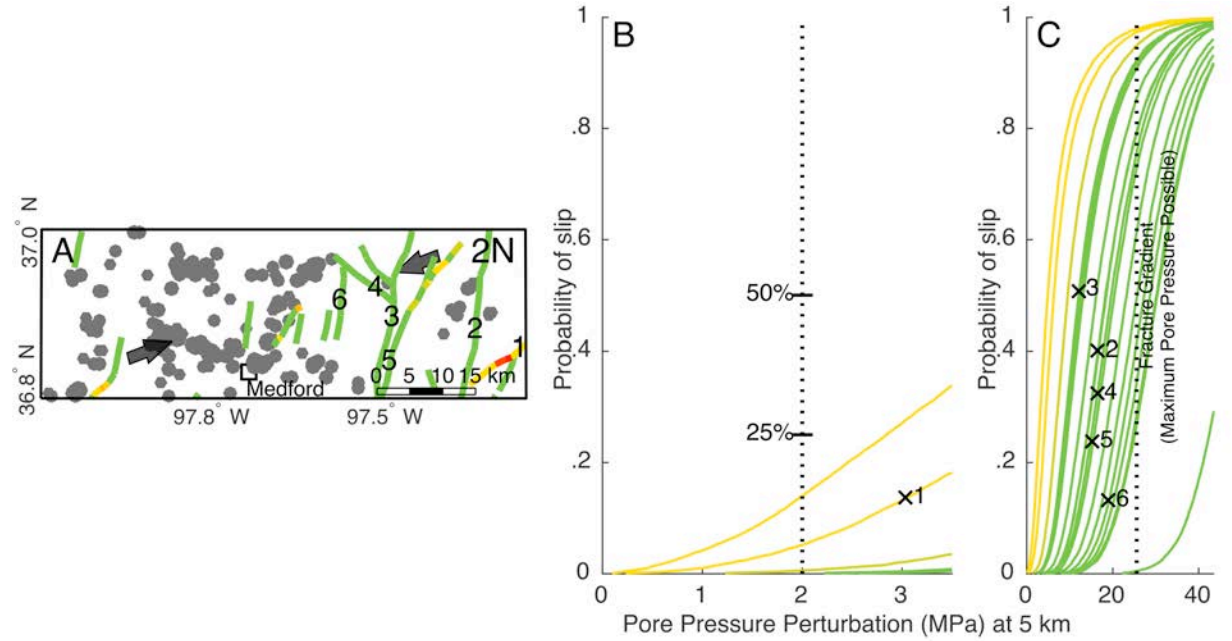

Figure DR15. Faults, NEIC earthquakes (A), and CDF curves (B, C) for area 2N.

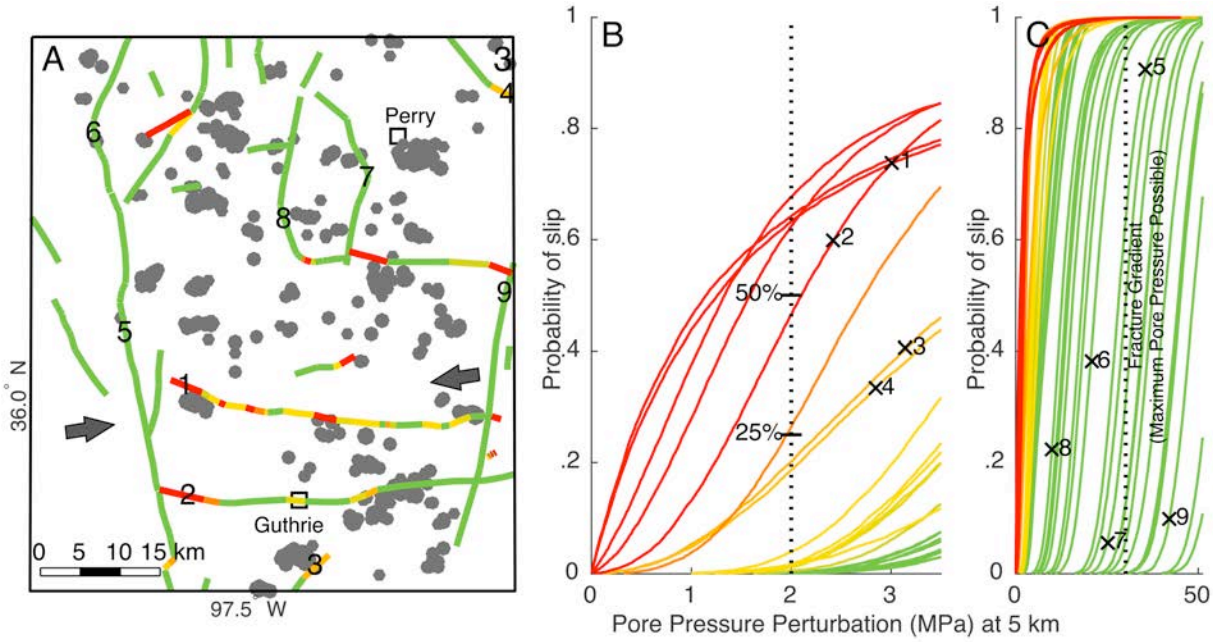

Figure DR16. Faults, NEIC earthquakes (A), and CDF curves (B, C) for area 3.

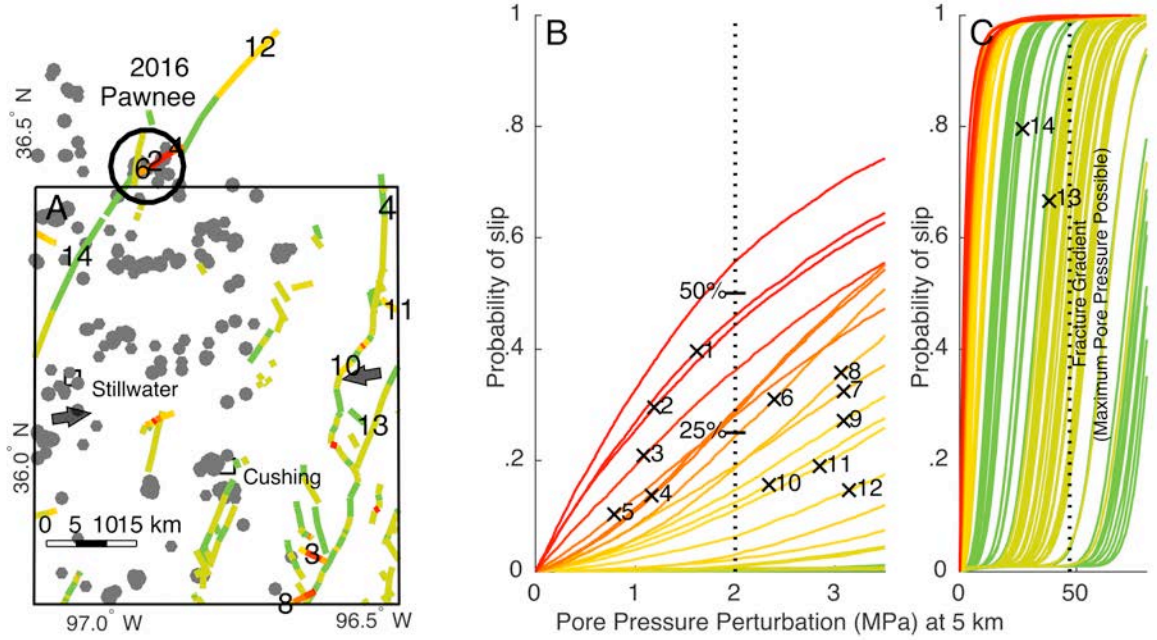

Figure DR17. Faults, NEIC earthquakes (A), and CDF curves (B, C) for area 4. The September 2016 Pawnee Magnitude 5.8 happened near a mapped fault just outside of area 4. When extend the area 4 analysis, we see fault segments 6, 2, and 4, from south to north, colored varying shades of orange and red. Their CDF curves are numbered correspondingly in panel B. Note that

this analysis is done with earthquakes up to 2 months before the magnitude 5.8, so it was not used in the inversion. The main event occurred on an unmapped fault conjugate to the mapped fault. Had it been mapped, it would have been colored red too.

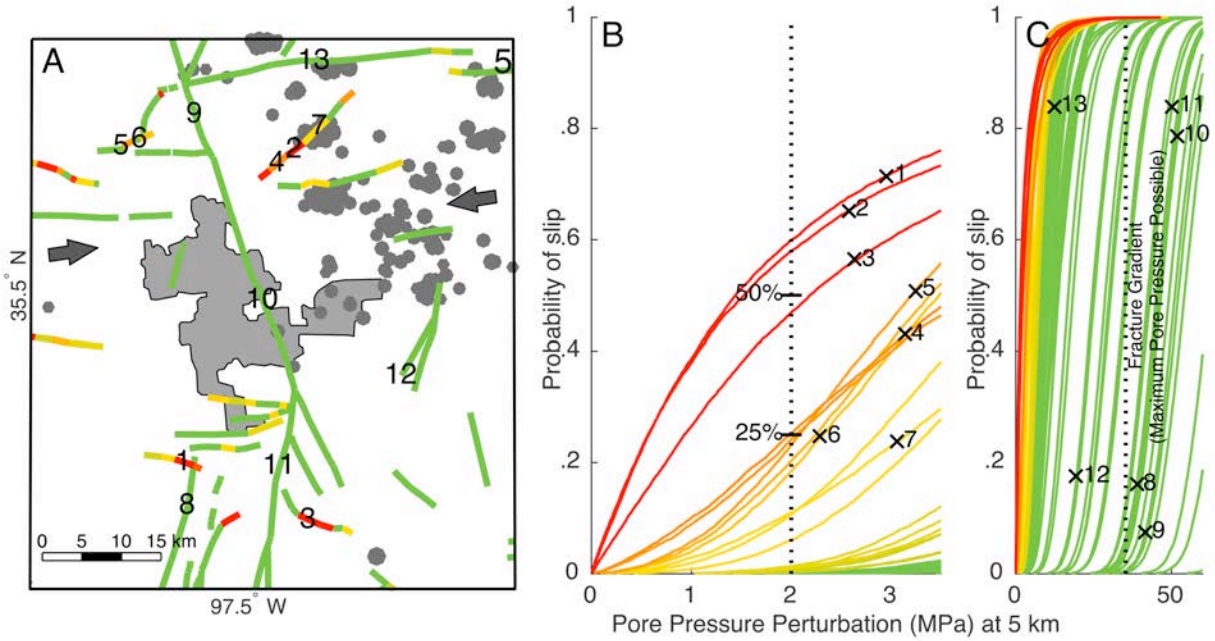

Figure DR18. Faults, NEIC earthquakes (A), and CDF curves (B, C) for area 5. The Oklahoma City urban area is outlined in grey.

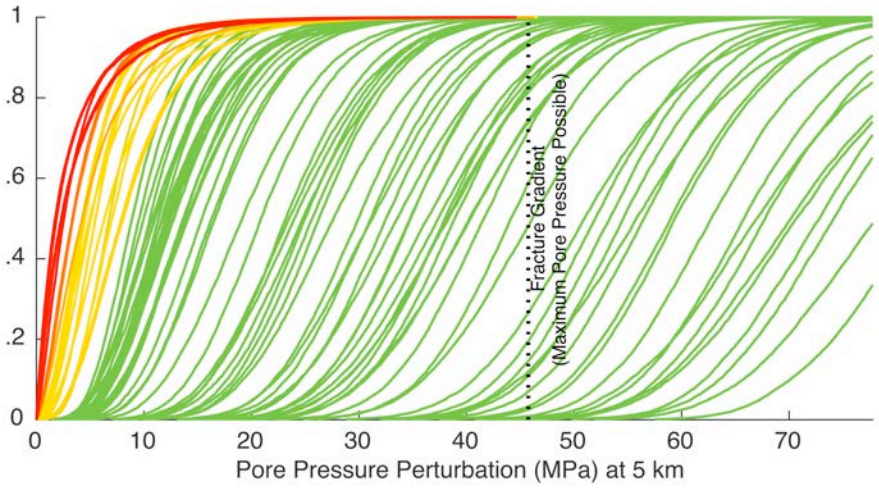

Figure DR19. CDF curves for study area 6 on an extended pressure axis.

REFERENCES CITED

Blanpied, M. L., Lockner, D. A., Byerlee, J. D., 1995, Frictional slip of granite at hydrothermal conditions: Journal of Geophysical Research v. 100, no. B7, p. 13,045-13,064.

Friberg, P. A., Besana-Ostman, G. M., and Dricker, I., 2014, Characterization of an earthquake sequence triggered by hydraulic fracturing in Harrison County, Ohio: Seismological Research Letters v. 85, no. 6 doi: 10.1785/0220140127

Ellsworth, W. L. 2013, Injection-induced earthquakes: Science, 12 Jul, 2013: V. 341: I. 6142. DOI: 10.1126/science.1225942

Holland, A. A., 2013 Earthquakes triggered by hydraulic fracturing in south-central Oklahoma: Bulletin of the Seismological Society of America v. 103, no. 3 p. 1784-1792.

Nelson, P. H., Gianoutsos, N. J., and Drake II, R. M., 2015, Underpressure in Mesozoic and Paleozoic rock units in the Midcontinent of the United States: AAPG Bulletin, v. 99, no. 10 pp. 1861–1892, DOI: 10.1306/04171514169.

NRC (National Research Council), *Induced Seismicity Potential in Energy Technologies* (The National Academies Press, Washington, DC, 2012).

Twiss, R.J., and Moores, E. M., 1992, Structural Geology, W. H. Freeman and company, 532 p.